A dielectric-defined lateral heterojunction in a monolayer semiconductor

M. Iqbal Bakti Utama[1,2,3,†], Hans Kleemann[1,4,†], Wenyu Zhao[1], Chin Shen Ong[1,3], Felipe H. da Jornada[1,3], Diana Y. Qiu[1,3], Hui Cai[5], Han Li[5], Rai Kou[1], Sihan Zhao[1], Sheng Wang[1,3], Kenji Watanabe[6], Takashi Taniguchi[6], Sefaattin Tongay[5], Alex Zettl[1,3,7], Steven G. Louie[1,3], Feng Wang[1,3,7,*]

[1] Department of Physics, University of California at Berkeley, Berkeley, California 94720, USA.
[2] Department of Materials Science and Engineering, University of California at Berkeley, Berkeley, California 94720, USA.
[3] Materials Science Division, Lawrence Berkeley National Laboratory, Berkeley, California, 94720, USA
[4] Institut für Angewandte Photophysik, Technische Universität Dresden, 01062 Dresden, Germany
[5] School for Engineering of Matter, Transport and Energy, Arizona State University, Tempe, Arizona 85287, United States
[6] National Institute for Materials Science, 1-1 Namiki, Tsukuba, 305-0044, Japan.
[7] Kavli Energy NanoSciences Institute at University of California Berkeley and Lawrence Berkeley National Laboratory, Berkeley, California 94720, United States.
[†] These authors contributed equally to this work
* To whom correspondence should be addressed: fengwang76@berkeley.edu

Abstract

Due to their low dimensionality, two-dimensional semiconductors, such as monolayer molybdenum disulfide, have a range of properties that make them valuable in the development of nanoelectronics. For example, the electronic bandgap of these semiconductors is not an intrinsic physical parameter and can be engineered through the dielectric environment around the monolayer. Here we show that this dielectric dependent electronic bandgap can be used to engineer a lateral heterojunction within a homogeneous MoS_2 monolayer. We visualize the heterostructure with Kelvin probe force microscopy and examine its influence on electrical transport experimentally and theoretically. We observe a lateral heterojunction with ~90 meV band offset due to different bandgap renormalization of monolayer MoS_2 when it is on a substrate in which one segment is made from an amorphous fluoropolymer (Cytop) and another segment from hexagonal boron nitride. This heterostructure leads to a diode-like electrical transport with a strong asymmetric behaviour.

Atomically thin semiconductors, such as monolayer transition metal dichalcogenides (TMDs)[1-3], provide a platform for investigating nanoscale quantum phenomena[4-6] and have a range of potential applications in nanoelectronics[7-9]. A freestanding monolayer of a transition metal dichalcogenide experiences a reduced dielectric screening and an enhanced Coulomb interaction by virtue of its atomically thin structure. In contrast to bulk materials, electric field lines between charges inside a monolayer can extend substantially outside of the layer[10-12]. This leads to an ineffective intrinsic screening that enhances electronic interaction and leads to large exciton binding energies between 0.2–0.7 eV in these materials[10-18]. Furthermore, the electronic band structure of atomically thin 2D layers is not completely intrinsic to the material and can be strongly affected by the surrounding environment[13,19-23]. With both electron and hole experiencing the screening, the conduction and valence band edges shift in the opposite direction[12,13,21,23]. *Ab initio* calculations predict that there is a monotonic decrease of electronic bandgap energy with increasing dielectric screening, where the reduction of bandgap can reach the order of hundreds of meV relative to the bandgap of a freestanding monolayer[13,20,22,24-27]. Recent scanning tunnelling spectroscopy[13] and optical spectroscopy[20,22] studies provided evidence that the bandgap renormalization phenomenon in atomically thin 2D semiconductors can indeed be significant. Such bandgap renormalization may have a profound effect on electrical transport in atomically thin 2D semiconductors; yet, the effect has not been investigated thoroughly and its implications in the development of applications based on 2D materials remains unclear.

In this Article, we design lateral heterojunctions within a homogeneous MoS_2 monolayer exploiting the dielectric-dependent bandgap renormalization and explore its influence on electrical transport. We prepared a continuous monolayer MoS_2 which has a segment on a high-ε substrate and an adjacent segment on a low-ε substrate (Fig. 1a). Due to the different degree of renormalization of the electronic bandgap introduced by the two substrates on each segment, the monolayer MoS_2 forms an in-plane type-I heterojunction above the boundary of the two substrates (Fig. 1b,c). We used this sample configuration to perform Kelvin Probe Force Microscopy (KPFM) and electrical transport measurements across the heterojunction. KPFM[28,29] examines the local variation of surface potential across the device channel[30] and provides a direct determination of the band offset of the MoS_2 heterojunction from the dielectric engineering. Electrical measurements show that the presence of the heterostructure has a significant effect on electrical transport through the device, leading to a strong asymmetric rectification behaviour. The experimentally observed transport phenomena can also be qualitatively reproduced in a numerical simulation of the device, which exhibits several unique aspects arising from the atomically thin layers. Such dielectric-defined heterostructure behaviour can be important for understanding electrical transport behaviour in atomically thin 2D layers and provide a new approach for engineering 2D nanoelectronic devices[4,31].

Theoretical calculations[21,23,32,33] show that the change in the bandgap of the 2D layer due to dielectric screening effect by the substrate(s) is most dramatic when the 2D layer has a low intrinsic dielectric constant (ε). In addition, a high contrast from the dielectric screening environment involving a low-ε substrate and a high-ε substrate is desirable to introduce a significant change in the bandgap of the 2D layer at the heterojunction. We choose the fluoropolymer Cytop (ε = 2.0–2.1) and hBN ($\varepsilon(0) = 6.9$, $\varepsilon(\infty) = 5.0$ normal to c-axis[34]) to serve as the $\varepsilon_{\mathrm{low}}$ and $\varepsilon_{\mathrm{high}}$ substrates respectively. The fluoropolymer Cytop substrate is one of the materials with the lowest dielectric constant that still allows ease of processing and device fabrication. Meanwhile, the straight edges of as-exfoliated thin hBN flake provide a boundary that is atomically sharp for a well-defined junction area. Moreover, both Cytop[35] and hBN[36] are known to be insulating layer with a low density of surface trap states.

Heterojunction device design and electrical measurement

We transferred a monolayer of MoS_2 atop the boundary of an hBN flake on a Cytop film and then fabricated electrical contacts onto the monolayer to form a device channel that is perpendicular to the Cytop/hBN substrate boundary (Fig. 2a). The electrical measurements are then performed in 4-terminal configuration to minimize the influence of contacts. Fig. 2b shows the *I-V* measurement of the device for different back gate-source voltages (which we shall refer to as “gate voltage” for brevity) $V_{\mathrm{gs}} > 0$ V, which correspond to electron doping. With the MoS_2 segment on Cytop grounded, the device exhibited a rectification behavior that is reminiscent of a diode. This rectification behaviour is consistent with the expected type-I heterojunction formation drawn in Fig. 1c, where the MoS_2 segments above the $\varepsilon_{\mathrm{low}}$ and $\varepsilon_{\mathrm{high}}$ substrates have different electronic bandgap due to dielectric screening. This behaviour is similar to an n-n heterojunction with MoS_2 segment on Cytop (hBN) containing the depletion (accumulation) regime[37].

In comparison, the reference MoS_2 monolayer device on a uniform Cytop film exhibits linear Ohmic-like behaviour (Fig. 2c), suggesting that the rectification arises from the presence of the heterojunction at the boundary between high-ε and low-ε substrates. Furthermore, we also conducted control experiments with MoS_2 monolayer on a step edge of an hBN flake that otherwise supports a uniform dielectric environment (Supplementary Fig. 7). Such control device shows symmetric output curves, which also substantiates that the rectification cannot be attributed only to the presence of step edge (*e.g.*, strain-induced or otherwise) without introducing dielectric contrast.

A prominent feature of our MoS_2 heterojunction device behaviour is that the I-V curve at forward bias that is higher than $V_{\mathrm{ch}} \approx 0.1$ V is mostly linear. This behaviour is commonly found in a real diode, which can be described by a piecewise linear model with a "turn-on" voltage (V_{t}) before the device appears to be Ohmic-like[38]. The turn-on voltage is often correlated to the potential landscape of the diode (*e.g.*, built-in voltage in Si p-n diode), and it provides an estimate of conduction band offset across the heterojunction. Our low-temperature transport measurements yield a turn-on voltage $V_{\mathrm{t}} \sim 90$ mV in the device (17 K, Fig. 2d).

KPFM characterization

Fig. 3a illustrates the KPFM measurement configuration, where lift mode with a constant tip height (h = 30 nm) is used and the DC component of bias voltage (V_{bias}) is applied to the sample. Fig. 3b displays the topography scan of atomic force microscope (AFM) from the MoS_2 heterojunction area at the Cytop/hBN substrate boundary. The averaged height profile (Fig. 3c) shows that the thickness of the hBN is around 10 nm. The exposed top surface in our devices allows for direct KPFM characterization.

As KPFM typically requires the sample to be sufficiently conducting, we performed KPFM on the MoS_2 when it is electrostatically gated to its on-state (electron accumulation) at high gate voltage. Fig. 3d shows the map of V_{bias} that was applied to the sample to cancel the electrostatic force between the tip and the sample, which is imaged at V_{gs} = 50 V. Meanwhile, Fig. 3e shows the corresponding averaged V_{bias} profile. The V_{bias} magnitude is related to the work function of the sample and that of the tip by $W_{f,\mathrm{sample}} = eV_{\mathrm{bias}} + W_{f,\mathrm{tip}}$ (see Supplementary Fig. 8). Therefore, the difference in local work function between two segments of the sample that are imaged by the same tip is given by:

$$\Delta W_{f,\mathrm{sample}} = e\Delta V_{\mathrm{bias}} \tag{1}$$

Two distinct areal regions of V_{bias} are seen in Fig. 3d that correlates well with the two segments of MoS_2 on Cytop and hBN from the topographic image (Fig. 3b). By using the averaged line profile in Fig. 3e, we therefore conclude that the work function difference ($\Delta W_f = W_{f,\mathrm{low}} - W_{f,\mathrm{high}}$) of MoS_2 on the Cytop and hBN substrate is -90 ± 20 meV at V_{gs} = 50 V. Here, the negative sign means that the vacuum level of MoS_2 on Cytop is lower than that on hBN.

The conduction band offset can be obtained from the work function difference by

$$\Delta E_c = -\Delta W_f - kT \ln\left[\frac{\exp\left(\frac{\pi\hbar^2 n_{\mathrm{low}}}{m^* kT}\right)-1}{\exp\left(\frac{\pi\hbar^2 n_{\mathrm{high}}}{m^* kT}\right)-1}\right] \tag{2}$$

with the carrier density $n = C_g\left(V_{gs} - V_{th}\right)/e$, where V_{th} is the gate threshold voltage, and m^* is the effective mass of electrons. Because the serial gate capacitance (C_g) at $\varepsilon_{\mathrm{high}}$ and $\varepsilon_{\mathrm{low}}$ side of the device does not differ significantly (the geometric capacitance of the 285 nm SiO_2 substrate dominates the serial capacitance), the ratio $n_{\mathrm{low}}/n_{\mathrm{high}}$ becomes closer to unity at high gate voltage. Applying these considerations to equation (2) in combination with (1) suggests that performing the measurement at the high gate voltage provides two major benefits: first, it counters the doping contribution from the environment to allow the relative carrier density on both sides of the junction to be more balanced since the charge density is dominated by that induced by the gate. Secondly, as the consequence of $n_{\mathrm{low}}/n_{\mathrm{high}} \approx 1$, KPFM measurements at high gate

146 voltage allow direct interpretation of the conduction band offset from the V_{bias} contrast. Fig. 3e therefore
147 implies that $\Delta E_c \approx -e\Delta V_{\text{bias}} \sim 90$ meV for our experimental condition, *i.e.*, E_c for MoS_2 on Cytop is
148 positioned higher than that on hBN.
149
150 The heterojunction measured by KPFM is consistent with the electrical transport data. It suggests that
151 dielectric engineered bandgap difference is around $\Delta E_g \approx 2\Delta E_C =$ -180±40 meV (illustrated in Fig. 1c),
152 assuming electron-hole symmetry. We compare this experimental result with the theoretical calculation of
153 the electronic bandgap of MoS_2 within the *ab initio* GW_0 approach as implemented in the BerkeleyGW
154 package[39-41] and account for the dielectric screening effect from the substrates using the in-plane substrate
155 averaging approach (details regarding the GW_0 calculation is in Supplementary Note 4)[13,33]. The GW_0
156 calculation shows that the bandgap of MoS_2 on a similar dielectric fluoropolymer as Cytop, after accounting
157 of surface roughness (Supplementary Fig. 3), is larger than that of MoS_2 on hBN by 120±40 meV, of which
158 the CBM offset is ~70±20 meV (Fig. 3f). Our calculations reveal that the roughness of the Cytop surface
159 decreases the effective dielectric screening experienced by MoS_2; the same calculation performed on a
160 perfectly smooth Cytop-like substrate results in a CBM offset of ~40 meV. The calculated bandgap and CBM
161 offset agree well with the experimental results, with overlapping error bars. The CBM and VBM offsets are
162 also approximately symmetric.
163

164 ## Energy band modelling

165 We model the electrical potential and charge transport through the junction numerically to understand the
166 unusual electrical transport from an atomically thin 2D heterojunction. While the rectification behaviour of
167 the heterojunction is consistent with the predicted band alignment in Fig. 1c, the transport data cannot be
168 aptly modelled with a thermionic emission theory commonly used to describe a Schottky diode, in which the
169 current level predicted from a thermionic emission mechanism is several orders of magnitude larger than that
170 measured herein (Supplementary Note 1 and Supplementary Fig. 1-2). The thermionic emission model fails
171 in atomically thin 2D layers because these 2D materials tend to have rather low mobility, and the drift-
172 diffusion behaviour of charge carriers plays a dominant role in the transport across the heterojunction[37]. To
173 accurately model the device behaviour, we introduce a carrier density dependent electron mobility in MoS_2
174 by $\mu(n) = \mu_0/[1 + \exp(\alpha^{-n+n_0})]$. Here, the mobility has a constant value of μ_0 at high doping but drops
175 significantly at low doping. This functional form is reminiscent to an activated behaviour with a certain
176 density of trap states, and the relevant parameters are obtained through gate-dependent transport data from a
177 homogeneous MoS_2 monolayer (Supplementary Fig. 5f-g). The density-dependent mobility is especially
178 relevant at the depletion region, which would experience increased local electrical resistance due to lowered
179 carrier density (Fig. 4d).
180
181 Fig. 4 shows the calculated band diagram and the associated band bending of MoS_2 around the Cytop and
182 hBN substrates for the conduction band edges at zero, forward, and reverse applied bias (see method in
183 Supplementary Note 2). The electron density n_0 at $x < 0$ (at Cytop) is assumed to be ~2×10^{12} cm^{-2}. The zero
184 bias calculation result (Fig. 4a) captures the built-in potential on each side of the junction (ψ_1 and ψ_2 for
185 MoS_2 on hBN and Cytop, respectively) because of the work function differences between the two segments
186 of MoS_2. In the case of a biased channel, the current flow is a response of a voltage drop over the whole
187 channel: $V_{ch} = E_F(z = -L) - E_F(z = L))$ that shifts the Fermi level out of equilibrium. However, we see
188 from both Fig. 4b and 4c that the voltage drop primarily transpires at the heterojunction, ensuring that the
189 heterojunction property to define the *I-V* behaviour of the device.
190
191 In the forward bias (Fig. 4b), the voltage drop across the heterojunction reduces the net built-in potential into
192 $\psi_1 - V_1$ and $\psi_2 - V_2$, respectively. A net current will flow with the electrons moving from the segment on
193 Cytop to that on hBN. At a finite temperature, electrons moving in this direction will see an energy barrier
194 for transport across the heterojunction. However, this energy barrier becomes negligible at a sufficiently
195 large applied bias $V_{ch} > V_t$, as illustrated in Fig. 4b. In other words, $\psi_2 - V_2 \approx 0$ and the transport across the
196 junction should be mostly dominated by the sheet resistance of MoS_2 away from the junction and appears
197 Ohmic-like. As an approximation, the $\psi_2 - V_2 \approx 0$ condition is achieved when the total built-in voltage
198 across the junction: $\psi_i = \psi_1 + \psi_2 \approx V_t$. We believe that this picture might explain the *I-V* behaviour for the
199 heterojunction as discussed in Fig. 2. An equivalent diode circuit for the junction is shown in the inset of Fig.
200 4b: the heterojunction is comprised of an internal built-in potential V_t that needs to be compensated by
201 applying an external potential, following which the current-voltage behaviour is dictated by a resistance R_s

in series due to the MoS_2 segment away from the junction. Our simulated *I-V* plot (Fig. 4e) reproduces the threshold-like behavior of the device.

Conclusions

We have reported an operational device application of bandgap renormalization in 2D materials via dielectric screening, and shown that a dielectric-engineered lateral heterojunction can strongly modify electrical transport in monolayer MoS_2. Since heterostructures are fundamental building blocks in electronics, such dielectric engineering can provide a powerful new route for realizing more complex device architecture. Our findings also have implications for the efforts to incorporate 2D materials in optoelectronics, in order to improve functionality (for example, spin-valley current for information encoding[42]) and drive miniaturization[43,44].

In practical applications, all aspects of manufacturing must be considered. For instance, the monolithic integration of 2D materials in circuitry requires interfacing with other components, such as substrate, electrodes, and interconnections. Each component may screen the 2D materials, resulting in different degree of bandgap renormalization across the channel. Notably, the bandgap of MX_2 should decrease significantly upon interfacing with electrodes due to the high permittivity of metals and thus a heterojunction is expected to form at each border between the MX_2 segments with and without metal contact. Although the behaviour of metal-MX_2 junction is dominated by other mechanisms such as Fermi-level pinning[45,46], recent work suggests the possibility to prevent pinning by minimizing disorders and interface states at the metal-MX_2 junction[47,48]. At such limit, accounting for bandgap renormalization is essential to fully understand the physics of electrical contact to MX_2 monolayers.

Although we have used Cytop and hBN substrates in order to simplify fabrication, the bandgap renormalization is a general phenomenon in 2D semiconductors and the heterojunction should form with other combinations of dielectrics. The constraint for low ε_{low} substrate may be satisfied by other established materials in industry, such as electronic-grade plastic substrates[49,50] with well-developed scalability and processability. Additionally, an advantage of such polymeric surfaces is the absence of dangling bonds, leading to a low density of surface trap sites. If conventional high-ε dielectrics are used, an abrupt heterojunction is affordable by patterning with state-of-the-art microfabrication technology. Another scalable approach also includes using CVD-grown 2D lateral heterojunction as the substrate if the material combination has a significant dielectric contrast[51,52]. We also believe that the influence from interface trapping and substrate doping for non-optimized surface can be minimized if the heterojunction is operated at high carrier density as defined by the electrostatic gating, where the difference in the work functions between low- and high-ε channel segments are primarily due to the bandgap renormalization.

Methods

Device fabrication. Cytop (CYTOP CTL-809M, Asahi Glass Co.) is mixed into CTL180 (Asahi Glass Co.) in 2:7 v/v and spincoated at 1000 rpm for 1 min to a uniform thickness of ~70 nm on highly doped Si substrates with 285 nm SiO_2. The Cytop-coated substrate is then heated at a hotplate for 5 min at 100°C and then 5 min at 150°C. Crystal of hBN is then exfoliated on the Cytop surface. The hBN flakes with thickness of 5-15 nm that have a flat side edge are identified from optical microscopy and confirmed with AFM imaging. Monolayers of MoS_2 are exfoliated onto a PDMS stamp and dry-transferred[53,54] to the flat edge of such hBN flake (Supplementary Fig. 4a,b). For all devices, 100 nm Au film is deposited for the electrode of MoS_2 using a standard electron beam lithography (EBL) process with two layers of EBL resist (495PMMA A4 and 950PMMA A4, MicroChem). We found that exposing the Cytop film to a short, low power N_2 plasma (10 sccm, 5 W for 1 s) before the hBN exfoliation can help to produce better spincoating of the resists on Cytop.

256 **KPFM.** KPFM were performed using a Multimode AFM with grounded tip and biased sample. A blunted Si
257 cantilever with ~50 nm Au film coating was used for the imaging. The measurement was performed in
258 surface potential mode with a lift-height of 30 nm and a drive amplitude of 2 V. The high lift-height was
259 chosen to avoid interaction between the metal tip and the monolayer MoS_2 that can introduce additional
260 screening effect. The AFM instrument is housed inside a home-made enclosure that is flushed with a
261 constant flow of dry nitrogen to provide an inert atmosphere.

262

263 Data availability

264 The data that support the plots within this paper and other findings of this study are available from the corre-
265 sponding author upon reasonable request

266

267 References

268 1. Wang, Q.H., Kalantar-Zadeh, K., Kis, A., Coleman, J.N. & Strano, M.S. Electronics and optoelectronics of two-
269 dimensional transition metal dichalcogenides. *Nature Nanotech.* **7**, 699-712 (2012).
270 2. Butler, S.Z. *et al.* Progress, challenges, and opportunities in two-dimensional materials beyond graphene. *ACS*
271 *Nano* **7**, 2898-2926 (2013).
272 3. Xia, F., Wang, H., Xiao, D., Dubey, M. & Ramasubramaniam, A. Two-dimensional material nanophotonics.
273 *Nature Photonics* **8**, 899 (2014).
274 4. Radisavljevic, B. & Kis, A. Mobility engineering and a metal–insulator transition in monolayer MoS_2. *Nature*
275 *Mater.* **12**, 815-820 (2013).
276 5. Mak, K.F., McGill, K.L., Park, J. & McEuen, P.L. The valley hall effect in MoS_2 transistors. *Science* **344**, 1489-
277 1492 (2014).
278 6. Cui, X. *et al.* Multi-terminal transport measurements of MoS_2 using a van der Waals heterostructure device
279 platform. *Nature Nanotech.* **10**, 534-540 (2015).
280 7. Fiori, G. *et al.* Electronics based on two-dimensional materials. *Nature Nanotech.* **9**, 768 (2014).
281 8. Jariwala, D., Sangwan, V.K., Lauhon, L.J., Marks, T.J. & Hersam, M.C. Emerging device applications for
282 semiconducting two-dimensional transition metal dichalcogenides. *ACS Nano* **8**, 1102-1120 (2014).
283 9. Chhowalla, M., Jena, D. & Zhang, H. Two-dimensional semiconductors for transistors. *Nature Rev. Mater.* **1**,
284 16052 (2016).
285 10. Qiu, D.Y., da Jornada, F.H. & Louie, S.G. Optical spectrum of MoS_2: Many-body effects and diversity of exciton
286 states. *Phys. Rev. Lett.* **111**, 216805 (2013).
287 11. Chernikov, A. *et al.* Exciton binding energy and nonhydrogenic rydberg series in monolayer WS_2. *Phys. Rev. Lett.*
288 **113**, 076802 (2014).
289 12. Qiu, D.Y., da Jornada, F.H. & Louie, S.G. Screening and many-body effects in two-dimensional crystals:
290 Monolayer MoS_2. *Phys. Rev. B* **93**, 235435 (2016).
291 13. Ugeda, M.M. *et al.* Giant bandgap renormalization and excitonic effects in a monolayer transition metal
292 dichalcogenide semiconductor. *Nature Mater.* **13**, 1091-1095 (2014).
293 14. Ye, Z. *et al.* Probing excitonic dark states in single-layer tungsten disulphide. *Nature* **513**, 214 (2014).
294 15. Zhang, C., Johnson, A., Hsu, C.-L., Li, L.-J. & Shih, C.-K. Direct imaging of band profile in single layer MoS_2 on
295 graphite: Quasiparticle energy gap, metallic edge states, and edge band bending. *Nano Lett.* **14**, 2443-2447 (2014).
296 16. Zhu, B., Chen, X. & Cui, X. Exciton binding energy of monolayer WS_2. *Sci. Rep.* **5**, 9218 (2015).
297 17. Hill, H.M. *et al.* Observation of excitonic rydberg states in monolayer MoS_2 and WS_2 by photoluminescence
298 excitation spectroscopy. *Nano Lett.* **15**, 2992-2997 (2015).
299 18. Zhang, Y. *et al.* Electronic structure, surface doping, and optical response in epitaxial WSe_2 thin films. *Nano Lett.*
300 **16**, 2485-2491 (2016).
301 19. Komsa, H.-P. & Krasheninnikov, A.V. Effects of confinement and environment on the electronic structure and
302 exciton binding energy of MoS_2 from first principles. *Phys. Rev. B* **86**, 241201 (2012).
303 20. Stier, A.V., Wilson, N.P., Clark, G., Xu, X. & Crooker, S.A. Probing the influence of dielectric environment on
304 excitons in monolayer WSe_2: Insight from high magnetic fields. *Nano Lett.* **16**, 7054-7060 (2016).
305 21. Ryou, J., Kim, Y.-S., Kc, S. & Cho, K. Monolayer MoS_2 bandgap modulation by dielectric environments and
306 tunable bandgap transistors. *Sci. Rep.* **6**, 29184 (2016).
307 22. Raja, A. *et al.* Coulomb engineering of the bandgap and excitons in two-dimensional materials. *Nature Commun.*
308 **8**, 15251 (2017).
309 23. Cho, Y. & Berkelbach, T.C. Environmentally-sensitive theory of electronic and optical transitions in atomically-
310 thin semiconductors. *Phys. Rev. B* **97**, 041409(R) (2018).
311 24. Bradley, A.J. *et al.* Probing the role of interlayer coupling and coulomb interactions on electronic structure in few-
312 layer $MoSe_2$ nanostructures. *Nano Lett.* **15**, 2594-2599 (2015).
313 25. Andersen, K., Latini, S. & Thygesen, K.S. Dielectric genome of van der Waals heterostructures. *Nano Lett.* **15**,
314 4616-4621 (2015).

315 26. Latini, S., Olsen, T. & Thygesen, K.S. Excitons in van der Waals heterostructures: The important role of dielectric
316 screening. *Phys. Rev. B* **92**, 245123 (2015).
317 27. Olsen, T., Latini, S., Rasmussen, F. & Thygesen, K.S. Simple screened hydrogen model of excitons in two-
318 dimensional materials. *Phys. Rev. Lett.* **116**, 056401 (2016).
319 28. Nonnenmacher, M., O'Boyle, M.P. & Wickramasinghe, H.K. Kelvin probe force microscopy. *Appl. Phys. Lett.* **58**,
320 2921-2923 (1991).
321 29. Melitz, W., Shen, J., Kummel, A.C. & Lee, S. Kelvin probe force microscopy and its application. *Surf. Sci. Rep.*
322 **66**, 1-27 (2011).
323 30. Tosun, M. *et al.* MoS_2 heterojunctions by thickness modulation. *Sci. Rep.* **5**, 10990 (2015).
324 31. Forsythe, C. *et al.* Band structure engineering of 2D materials using patterned dielectric superlattices. *Nature*
325 *Nanotech.*, doi.org/10.1038/s41565-41018-40138-41567 (2018).
326 32. Li, L. *et al.* Direct observation of the layer-dependent electronic structure in phosphorene. *Nature Nanotech.* **12**,
327 21 (2016).
328 33. Qiu, D.Y., da Jornada, F.H. & Louie, S.G. Environmental screening effects in 2D materials: Renormalization of the
329 bandgap, electronic structure, and optical spectra of few-layer black phosphorus. *Nano Lett.* **17**, 4706-4712 (2017).
330 34. Geick, R., Perry, C.H. & Rupprecht, G. Normal modes in hexagonal boron nitride. *Phys. Rev.* **146**, 543-547
331 (1966).
332 35. Liu, B. *et al.* Engineering bandgaps of monolayer MoS_2 and WS_2 on fluoropolymer substrates by electrostatically
333 tuned many-body effects. *Adv. Mater.* **28**, 6457-6464 (2016).
334 36. Dean, C.R. *et al.* Boron nitride substrates for high-quality graphene electronics. *Nature Nanotech.* **5**, 722-726
335 (2010).
336 37. Sze, S.M. & Ng, K.K. *Physics of semiconductor devices*. (Wiley, 2007).
337 38. Sedra, A.S. & Smith, K.C. *Microelectronic circuits*. 5th edn, (Oxford University Press, 2004).
338 39. Hybertsen, M.S. & Louie, S.G. Electron correlation in semiconductors and insulators: Band gaps and quasiparticle
339 energies. *Phys. Rev. B* **34**, 5390-5413 (1986).
340 40. Deslippe, J. *et al.* Berkeleygw: A massively parallel computer package for the calculation of the quasiparticle and
341 optical properties of materials and nanostructures. *Comp. Phys. Comm.* **183**, 1269-1289 (2012).
342 41. da Jornada, F.H., Qiu, D.Y. & Louie, S.G. Nonuniform sampling schemes of the Brillouin zone for many-electron
343 perturbation-theory calculations in reduced dimensionality. *Phys. Rev. B* **95**, 035109 (2017).
344 42. Jin, C. *et al.* Imaging of pure spin-valley diffusion current in WS_2-WSe_2 heterostructures. *Science* **360**, 893-896
345 (2018).
346 43. Alam, K. & Lake, R.K. Monolayer MoS_2 transistors beyond the technology road map. *IEEE Trans. Elect. Dev.* **59**,
347 3250-3254 (2012).
348 44. Desai, S.B. *et al.* MoS_2 transistors with 1-nanometer gate lengths. *Science* **354**, 99-102 (2016).
349 45. Das, S., Chen, H.-Y., Penumatcha, A.V. & Appenzeller, J. High performance multilayer MoS_2 transistors with
350 scandium contacts. *Nano Lett.* **13**, 100-105 (2013).
351 46. Giannazzo, F., Fisichella, G., Piazza, A., Agnello, S. & Roccaforte, F. Nanoscale inhomogeneity of the schottky
352 barrier and resistivity in MoS_2 multilayers. *Phys. Rev. B* **92**, 081307 (2015).
353 47. Cui, X. *et al.* Low-temperature ohmic contact to monolayer MoS_2 by van der Waals bonded Co/h-BN electrodes.
354 *Nano Lett.* **17**, 4781-4786 (2017).
355 48. Liu, Y. *et al.* Approaching the schottky–mott limit in van der Waals metal–semiconductor junctions. *Nature* **557**,
356 696-700 (2018).
357 49. Maier, G. Low dielectric constant polymers for microelectronics. *Prog. Polym. Sci.* **26**, 3-65 (2001).
358 50. Stoppa, M. & Chiolerio, A. Wearable electronics and smart textiles: A critical review. *Sensors* **14**, 11957 (2014).
359 51. Levendorf, M.P. *et al.* Graphene and boron nitride lateral heterostructures for atomically thin circuitry. *Nature* **488**,
360 627-632 (2012).
361 52. Liu, Z. *et al.* In-plane heterostructures of graphene and hexagonal boron nitride with controlled domain sizes.
362 *Nature Nanotech.* **8**, 119-124 (2013).
363 53. Castellanos-Gomez, A. *et al.* Deterministic transfer of two-dimensional materials by all-dry viscoelastic stamping.
364 *2D Mater.* **1**, 011002 (2014).
365 54. Lee, G.-H. *et al.* Flexible and transparent MoS_2 field-effect transistors on hexagonal boron nitride-graphene
366 heterostructures. *ACS Nano* **7**, 7931-7936 (2013).
367
368

369

370 # Acknowledgements

371 We thank M. Asta, J. Yao, and S. Kahn for helpful discussions. This work was primarily supported by the
372 Center for Computational Study of Excited State Phenomena in Energy Materials, which is funded by the
373 U.S. Department of Energy, Office of Science, Basic Energy Sciences, Materials Sciences and Engineering
374 Division under Contract No. DE-AC02-05CH11231, as part of the Computational Materials Sciences Pro-

375 gram. The device fabrication is supported by National Science Foundation EFRI program (EFMA-1542741).
376 This research used resources of the National Energy Research Scientific Computing Center (NERSC), a
377 DOE Office of Science User Facility supported by the Office of Science of the U.S. Department of Energy
378 under Contract No. DE-AC02-05CH11231, and the Extreme Science and Engineering Discovery Environ-
379 ment (XSEDE), which is supported by National Science Foundation grant number ACI-1548562. H.K. was
380 supported by the Deutsche Forschungsgemeinschaft (KL 2961/1-1). C.S.O. acknowledges support from the
381 Singapore National Research Foundation (Clean Energy) PhD Scholarship. R.K. was supported by the JSPS
382 Overseas Research Fellowship Program. S.T. acknowledges the support from NSF DMR 1552220 NSF CA-
383 REER award. Growth of hexagonal boron nitride crystals was supported by the Elemental Strategy Initiative
384 conducted by the MEXT, Japan and a Grant-in-Aid for Scientific Research on Innovative Areas 'Science of
385 Atomic Layers' from JSPS.

386

387 ## Author contribution

388 F.W., M.I.B.U., H.K. conceived the project and designed the experiments. M.I.B.U. and H.K. performed
389 sample preparation, device fabrication, electrical transport measurements, and data analysis. W.Z., M.I.B.U.,
390 and S.W. performed KPFM measurement. M.I.B.U. conducted optical spectroscopy. R.K., S.Z., and A.Z.
391 contributed in the device fabrication process. F.W., M.I.B.U., H.K. simulated the energy band diagram of the
392 heterojunction. C.S.O., F.H.d.J., and D.Y.Q. performed GW calculations on and together with S.G.L. did the
393 analyses of the quasiparticle band structures. H.C., H.L., and S.T. grown the MoS_2 single crystal. K.W. and
394 T.T. grew the hBN single crystal. F.W., S.G.L., and A.Z. supervised the project.

395

396 ## Financial and non-financial competing interests

397 The authors declare no competing interests.

398

399 ## Additional information

400 **Supplementary information** is available for this paper at https://doi.org/10.1038/xxxx.
401 **Reprints and permissions information** is available online at www.nature.com/reprints.
402 **Correspondence and requests for materials** should be addressed to F.W.
403 **Publisher's note:** Springer Nature remains neutral with regard to jurisdictional claims in published maps and
404 institutional affiliations.
405 © The Author(s), under exclusive licence to Springer Nature Limited 2019
406
407
408

Figure 1 | Engineering 2D heterojunction through dielectric-dependent bandgap renormalization. a, Schematic illustration of the heterostructure. Two substrates with different dielectric constant ($\varepsilon_{\mathrm{low}} < \varepsilon_{\mathrm{high}}$) are used to locally vary the MoS_2 electronic bandgap. **b,** The expected band alignment of isolated monolayer MoS_2 situated on $\varepsilon_{\mathrm{low}}$ substrate (Cytop) and on $\varepsilon_{\mathrm{high}}$ substrate (hBN), respectively. The segment of MoS_2 monolayer on Cytop and that on hBN are assumed to have the same electron doping density from the electrostatic gating. **c,** The band alignment from (**b**) if the MoS_2 segments at the two substrates are in contact and reach equilibrium following Anderson's rule. A type-I lateral heterojunction forms with an energy barrier for electron transport in the conduction band.

Figure 2 | Current-voltage characteristics of MoS_2 heterojunction device. a, Optical micrograph of an MoS_2 monolayer that is partially situated on Cytop and on hBN substrates. The white dashed line denotes the location of the monolayer that acts as the device channel. The MoS_2 segment on hBN received the high bias potential (drain). Scale bar: 2 μm. **b,** The output characteristics of the device with various back gating at the temperature of 200 K. **c,** The output characteristics of a reference MoS_2 monolayer device on a uniform Cytop substrate measured at 200 K. Inset: The micrograph of the reference device. Scale bar: 2 μm. **d,** The output characteristics of the heterojunction device at 17 K in log-log scale. The forward bias current is fitted with a straight line that extrapolates to a turn-on voltage of 90 mV. Inset: the same data in linear scale.

Figure 3 | KPFM characterization of the MoS_2 heterojunction formation from differences in the degree of local dielectric screening. a, Schematic of the KPFM setup with V_{bias} applied to the sample. For the measurements herein, the device is back gated to V_{gs} = 50 V and the lift height of the tip is set to h = 30 nm. **b,** The topography image recorded in tapping mode AFM. **c,** The height profile, averaged from the area inside the white-dashed rectangle in (**b**). **d,** The spatially mapped V_{bias} from the same area as in (**b**). **e,** The V_{bias} profile from (**d**), also averaged similarly from the same area as in (**c**). Given that $\Delta E_c = -e\Delta V_{\mathrm{bias}}$ in the measurement configuration, the KPFM result demonstrates that the conduction band edge of MoS_2 on Cytop substrate is higher by 90 meV than that of MoS_2 on hBN. **f,** Results from GW calculations of the bandgap and band alignment of monolayer MoS_2 that is freestanding without substrate screening effect (left), that is placed on a surface of a fluoropolymer (middle), and that is placed on a hBN substrate (Scale bars in (**b**) and (**d**) corresponds to 500 nm).

Figure 4 | Simulation results of the energy band bending at the 2D heterojunction. a,b,c The conduction band edges and Fermi levels are calculated at (**a**) zero bias, (**b**) forward biased (current: 80 nA/μm), and (**c**) reverse biased condition (current: -6 nA/μm). In the three cases, the MoS_2 segment on Cytop is assigned to be electrically grounded. Under small forward bias (V_{ch} = V_1 + V_2), an electron traversing the heterojunction from the segment on Cytop to that on hBN experiences an energy barrier due to the built-in voltage. However, for large enough bias beyond the turn-on voltage (V_{ch} > V_t), electrons traversing the heterojunction (blue circle) do not experience significant energy barrier and the current-voltage characteristic is determined by the resistance of the channel instead of the junction. Inset in (**b**): a schematic of the diode modelling according to piecewise linear model. **d,** Carrier density distribution across the junction under different bias condition. **e,** Simulated current-voltage characteristics with a carrier density-dependent mobility. All calculations are performed using carrier density of 2.0×10^{12} cm^{-2} at 140 K.

a

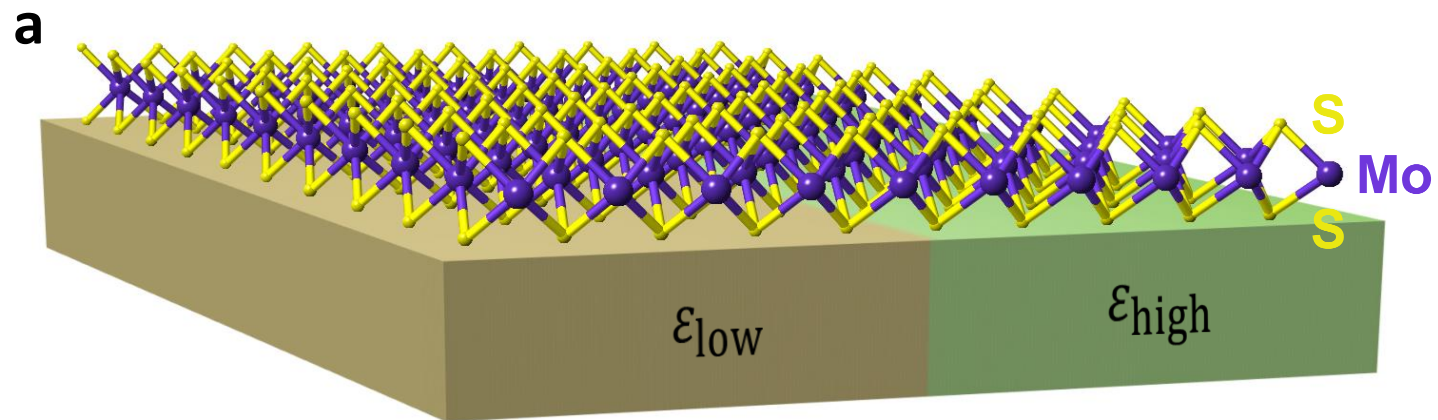

b

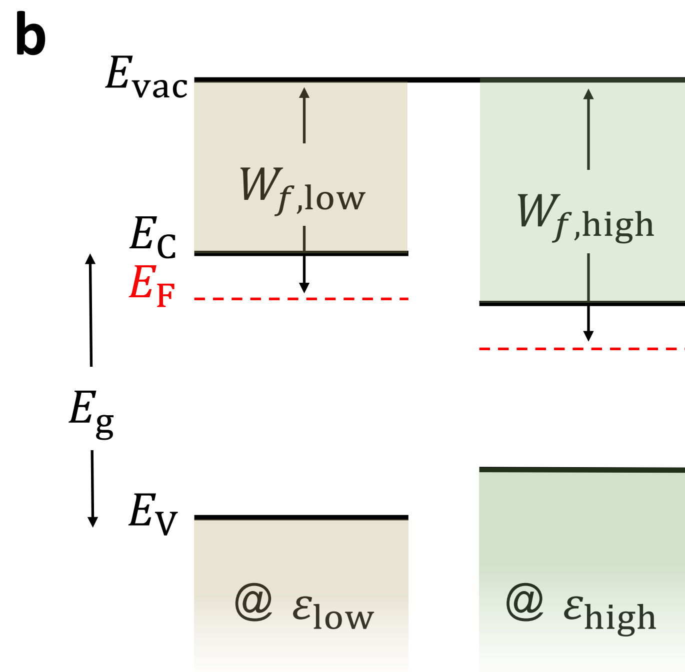

c

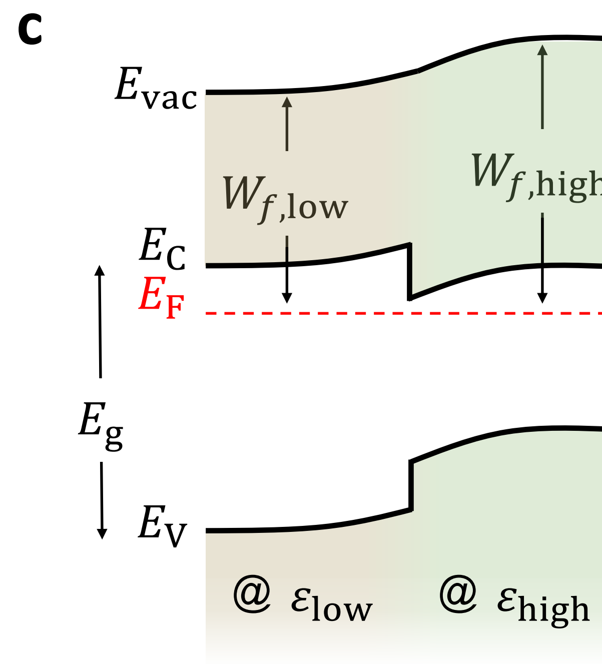

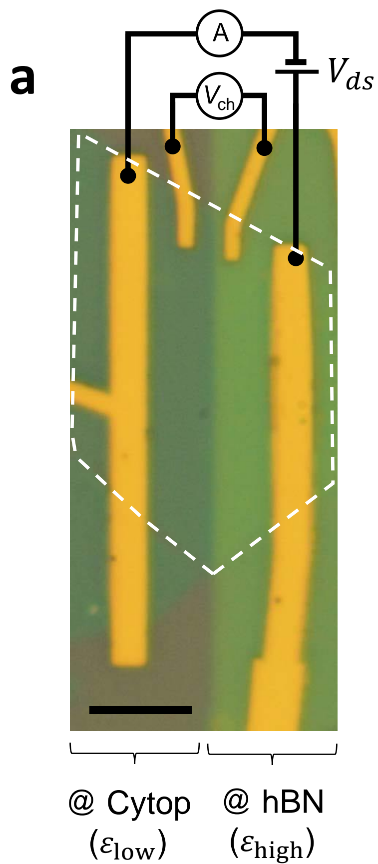
a
A
V_{ds}
V_{ch}
@ Cytop (ε_{low})
@ hBN (ε_{high})

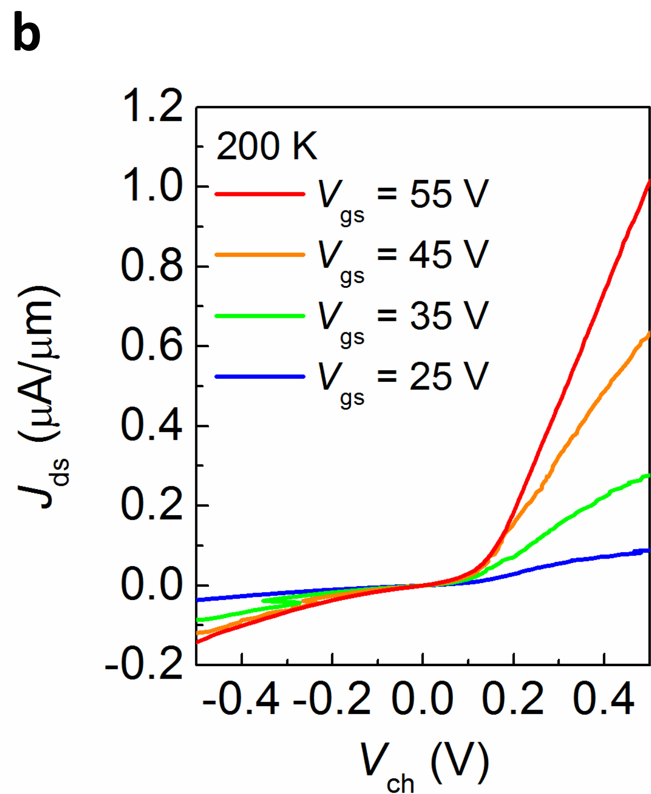
b
200 K
V_{gs} = 55 V
V_{gs} = 45 V
V_{gs} = 35 V
V_{gs} = 25 V
J_{ds} (μA/μm)
V_{ch} (V)

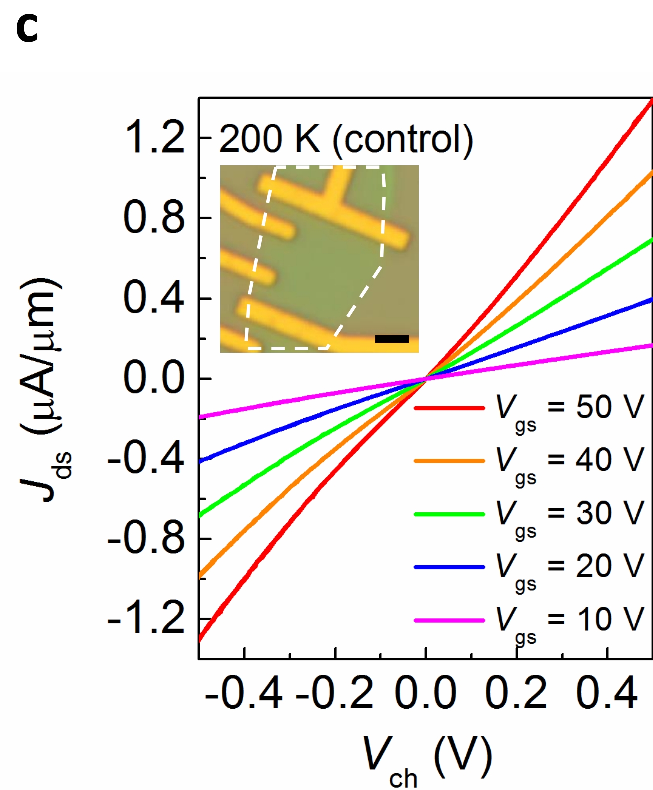
c
200 K (control)
V_{gs} = 50 V
V_{gs} = 40 V
V_{gs} = 30 V
V_{gs} = 20 V
V_{gs} = 10 V
J_{ds} (μA/μm)
V_{ch} (V)

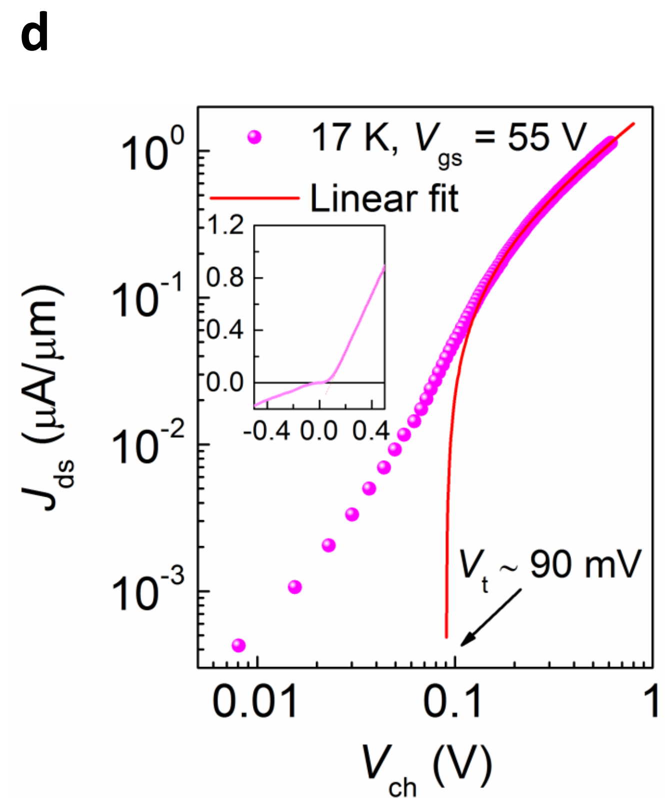
d
17 K, V_{gs} = 55 V
Linear fit
V_t ~ 90 mV
J_{ds} (μA/μm)
V_{ch} (V)

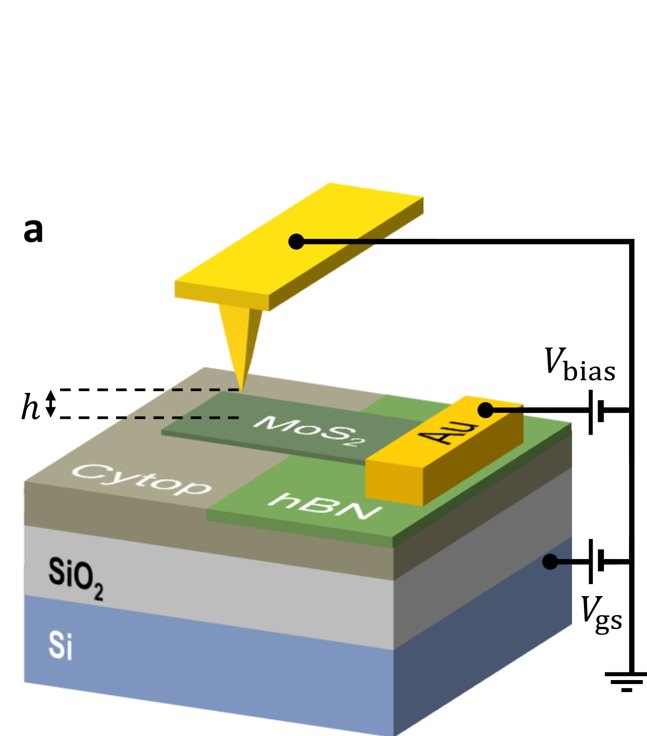
a
h
MoS$_2$
Au
Cytop
hBN
SiO_2
Si
V_{bias}
V_{gs}

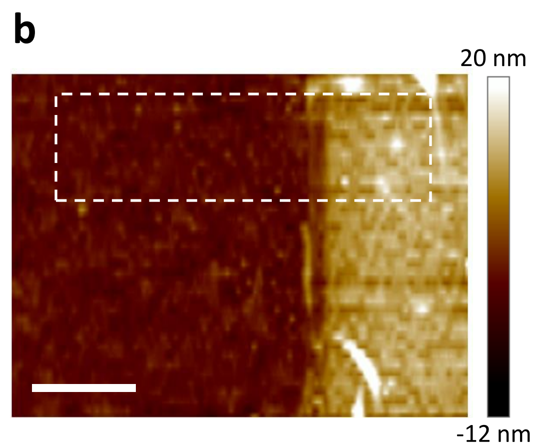
b
20 nm
-12 nm

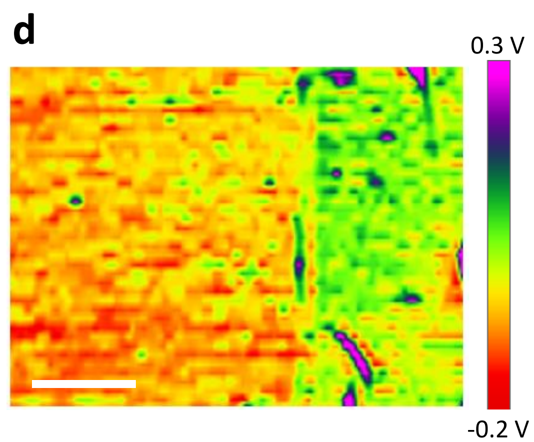
d
0.3 V
-0.2 V

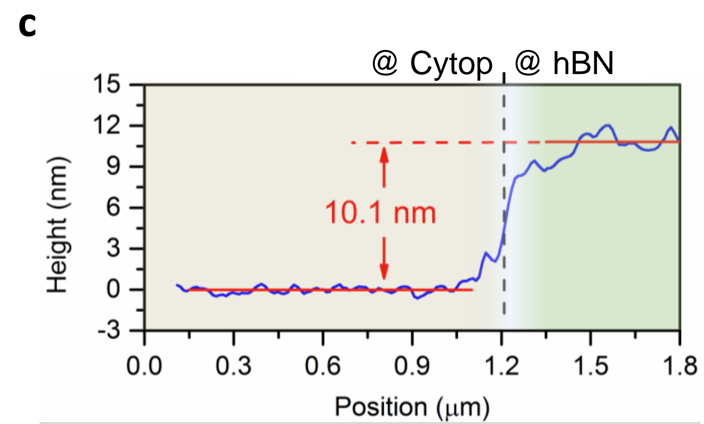
c
@ Cytop
@ hBN
10.1 nm
Height (nm)
Position (μm)

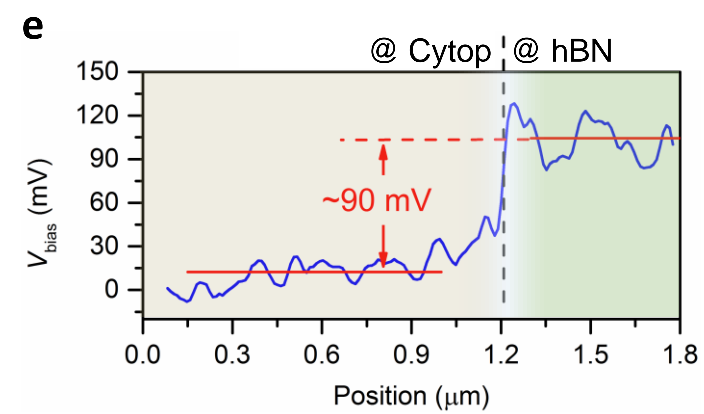
e
@ Cytop
@ hBN
~90 mV
V_{bias} (mV)
Position (μm)

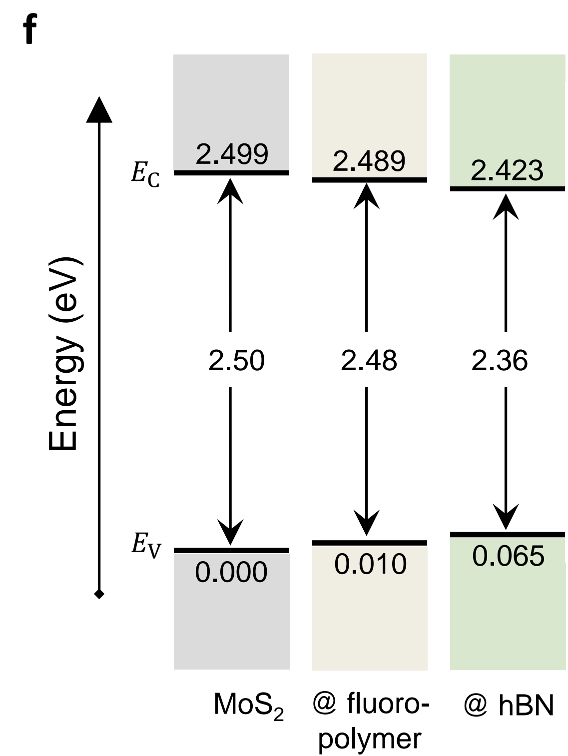
f
Energy (eV)
E_C
E_V
2.499
2.489
2.423
2.50
2.48
2.36
0.000
0.010
0.065
MoS$_2$
@ fluoro-polymer
@ hBN

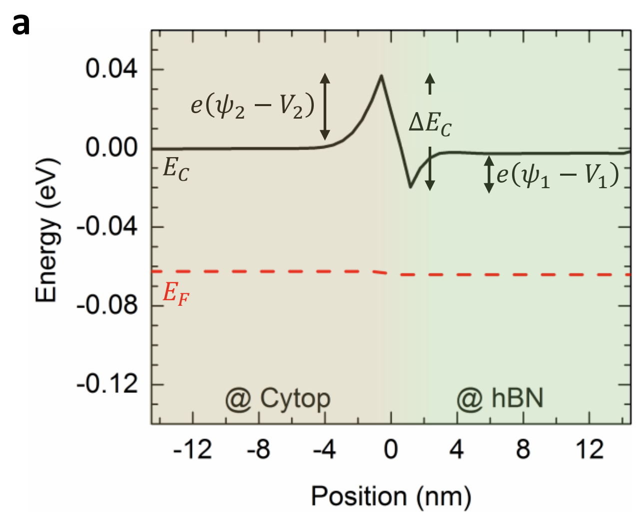
a
0.04
0.00
-0.04
-0.08
-0.12
Energy (eV)
$e(\psi_2 - V_2)$
ΔE_C
E_C
$e(\psi_1 - V_1)$
E_F
@ Cytop
@ hBN
-12 -8 -4 0 4 8 12
Position (nm)

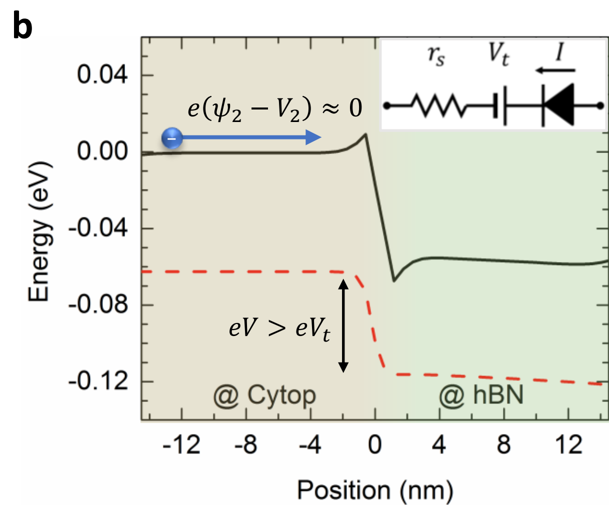
b
r_s
V_t
I
$e(\psi_2 - V_2) \approx 0$
$eV > eV_t$
Energy (eV)
@ Cytop
@ hBN
Position (nm)

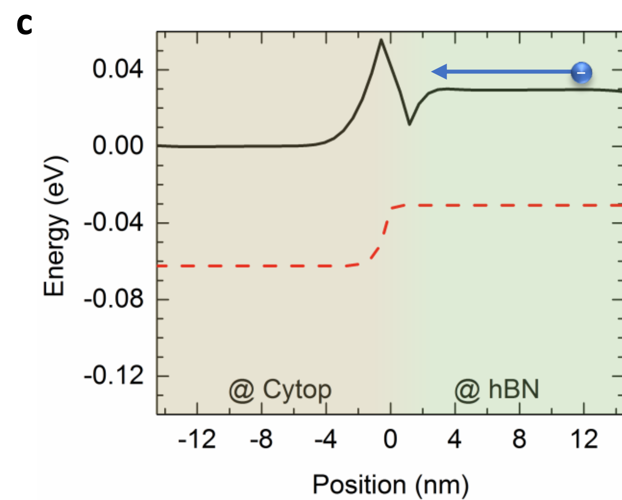
c
Energy (eV)
@ Cytop
@ hBN
Position (nm)

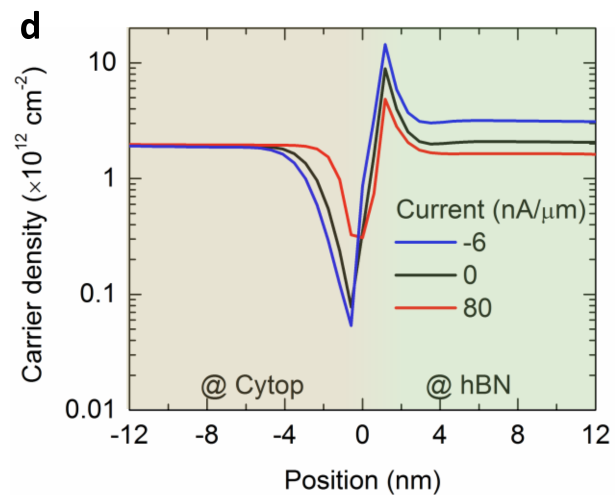
d
Carrier density ($\times 10^{12}$ cm^{-2})
Current (nA/μm)
-6
0
80
@ Cytop
@ hBN
Position (nm)

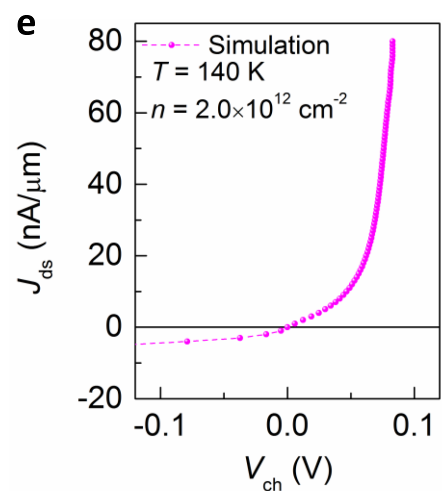
e
Simulation
T = 140 K
$n = 2.0\times10^{12}$ cm^{-2}
J_{ds} (nA/μm)
V_{ch} (V)